Accelerated Motion Corrected Three-Dimensional Abdominal MRI Using Total Variation Regularized SENSE Reconstruction

Gastao Cruz,[1]* David Atkinson,[2] Christian Buerger,[3] Tobias Schaeffter,[1] and Claudia Prieto[1,4]

Purpose: Develop a nonrigid motion corrected reconstruction for highly accelerated free-breathing three-dimensional (3D) abdominal images without external sensors or additional scans.
Methods: The proposed method accelerates the acquisition by undersampling and performs motion correction directly in the reconstruction using a general matrix description of the acquisition. Data are acquired using a self-gated 3D golden radial phase encoding trajectory, enabling a two stage reconstruction to estimate and then correct motion of the same data. In the first stage total variation regularized iterative SENSE is used to reconstruct highly undersampled respiratory resolved images. A nonrigid registration of these images is performed to estimate the complex motion in the abdomen. In the second stage, the estimated motion fields are incorporated in a general matrix reconstruction, which uses total variation regularization and incorporates k-space data from multiple respiratory positions. The proposed approach was tested on nine healthy volunteers and compared against a standard gated reconstruction using measures of liver sharpness, gradient entropy, visual assessment of image sharpness and overall image quality by two experts.
Results: The proposed method achieves similar quality to the gated reconstruction with nonsignificant differences for liver sharpness (1.18 and 1.00, respectively), gradient entropy (1.00 and 1.00), visual score of image sharpness (2.22 and 2.44), and visual rank of image quality (3.33 and 3.39). An average reduction of the acquisition time from 102 s to 39 s could be achieved with the proposed method.
Conclusion: In vivo results demonstrate the feasibility of the proposed method showing similar image quality to the standard gated reconstruction while using data corresponding to a significantly reduced acquisition time. **Magn Reson Med**

[1]King's College London, Division of Imaging Sciences and Biomedical Engineering, London, United Kingdom.

[2]Centre for Medical Imaging, University College London, London, United Kingdom.

[3]Philips Research Hamburg, Hamburg, Germany.

[4]Pontificia Universidad Católica de Chile, Escuela de Ingeniería, Santiago, Chile

*Correspondence to: Gastao Cruz, M.Sc., Division of Imaging Sciences and Biomedical Engineering, The Rayne Institute, 4th Floor, Lambeth Wing, St Thomas' Hospital, London, SE1 7EH, UK. E-mail: gastao.cruz@kcl.ac.uk

INTRODUCTION

Respiratory motion is a major source of artifacts in abdominal imaging, causing ghosting and blurring in the reconstructed image (1). In two dimensions, a simple approach to reduce these artifacts is to acquire the image during breathhold(s). Unfortunately, breathholding is difficult in three dimensions without compromising resolution/scan time; therefore, a three-dimensional (3D) free-breathing acquisition is desired. Free-breathing acquisition is usually performed using respiratory gating techniques (2). Respiratory gating monitors the position of the diaphragm in the superior–inferior (SI) direction using external sensors, navigator echoes or self-gating. External sensors require additional preparation and provide only a relative measurement of diaphragm displacement (3). Navigator echoes do not have these limitations, but can interfere with image acquisition (e.g., disrupting the balanced steady state free precession acquisition) (4). Self-gating techniques (5) extract motion information from the acquired data itself, in general using the central k-space profile. Respiratory gating only accepts data within a small gating window, minimizing motion artifacts at the expense of additional scan time. Moreover, in subjects with highly irregular breathing patterns, drift in respiratory motion can lead to scan termination due to low scan efficiency. Respiratory gating monitors SI translational motion, although it is known that abdominal acquisitions are corrupted by large nonrigid components of motion (6–8).

In cardiac imaging, several approaches have been proposed for motion compensation. In (9), SI motion is estimated by means of self-navigation, enabling the estimation of data weighting factors from the distance to a reference respiratory phase. This information is then used in a weighted iterative reconstruction with total variation regularization to reduce respiratory artifacts. More complex 3D affine motion has been estimated from 3D low resolution image navigators and used to correct the actual acquisition in image space (10). An alternative approach (11) estimates 3D affine motion

from respiratory resolved images and uses it to correct the acquired k-space before reconstructing the image. In Prieto et al (12), motion is estimated similarly, but is then corrected directly in the Cartesian reconstruction using the General Matrix Description (GMD) (13). Additional solutions have been proposed to correct the more complex nonrigid abdominal motion. A pixel-by-pixel translation correction has been used to correct nonrigid motion (14) using local autofocus (15). This technique requires the acquisition of additional navigator echoes as well as triggering and gating of a portion of the acquired data. A self-gated motion corrected approach is proposed in Buerger et al (16), where nonrigid motion is estimated from undersampled respiratory resolved images. A motion compensated image is then obtained by warping all undersampled images to a common respiratory position. However, this image-based approach has two major limitations: (i) aliasing artifacts of each undersampled motion state are warped to the common respiratory position and may persist in the final image, and (ii) the averaging of multiple motion states may lead to blurring in the final image. The latter effect has been shown for abdominal and cardiac images in (17,18) when compared with the GMD approach. GMD corrects motion directly during the reconstruction process; although a previous estimation of the motion is required. This motion has been estimated from low-resolution training acquisitions (19) or from a computationally expensive coupled motion reconstruction and motion estimation problem based on external sensors (20). These approaches have been demonstrated for fully and over-sampled acquisitions only. Here, we propose a highly accelerated GMD-based method to correct nonrigid motion in undersampled 3D isotropic abdominal images.

The motion estimation step of the proposed approach is an extension of the one used in (16) to account for undersampled acquisitions. Data are acquired under free breathing with a self-gated golden-radial phase encoding (G-RPE) trajectory (21,22), enabling the reconstruction of highly undersampled images at various motion states (respiratory bins). Unlike Buerger et al (16), where iterative SENSE reconstruction (23) was sufficient to independently reconstruct the bins, here we propose to reconstruct all motion states simultaneously using a spatial and temporal total variation regularized iterative SENSE (TV-SENSE) approach, allowing reliable motion estimation from bins with higher undersampling factors than those reported in (16). Additionally, in the proposed method motion compensation is performed directly in the reconstruction, incorporating parallel imaging information and spatial total variation regularization (TV-GMD). The proposed approach was tested on nine healthy volunteers and compared against a standard gated reconstruction.

METHODS

The proposed framework can be divided into five steps (Figs. 1b,c). In the first step, data are acquired with a self-gated 3D golden-radial phase encoding (G-RPE) trajectory during free breathing. These data are sequentially assigned into different motion states, yielding a set of highly undersampled k-spaces K_b at the completion of the acquisition (step 2). Each bin is reconstructed with TV-SENSE (step 3), producing undersampled respiratory resolved images I_b. In the next step, nonrigid motion is estimated using image registration of I_b. Finally, the estimated motion is used to reconstruct a motion corrected image using TV-GMD.

Image Acquisition

G-RPE (21,22) combines a regularly sampled Cartesian readout (k_x) in SI direction with a radial phase encoding order in the k_y-k_z plane, where radial profiles are separated by the golden angle $\theta_G = 111.25°$ (Figure 1a, top). A G-RPE acquisition can be undersampled radially by skipping readouts within each radial profile and angularly by acquiring fewer radial profiles (Figure 1a, bottom). This trajectory provides a quasi-uniform k-space distribution regardless of the number of profiles used (24), ensuring an optimal distribution of profiles in k-space for different length of data acquisition. Additionally, the central k-space readout (red line in Figure 1b) is acquired every N × TR seconds where is N the number of readouts within a radial profile and TR is the repetition time, allowing for respiratory self-navigation. If the acquisition time for the radial profile (N × TR) is fast enough, respiratory motion within the radial profile can be considered negligible and the central k-space readout can be used to navigate the entire radial profile.

Data Binning

We identify the respiratory position of each radial profile by inferring the diaphragm displacement in the (SI) read-out direction as described in Buerger et al (25). This self-navigated respiratory signal is used to group the acquired data into different respiratory positions. During this process, referred as data binning, the radial profiles in each bin will not be equally spaced by the golden angle as they depend on the breathing cycle (16). Therefore a quasi-uniform k-space distribution is not guaranteed for any bin. k-Space gaps may generate artifacts in I_b and affect subsequent motion estimation. Thus, it is important to ensure that each bin has adequate coverage of k-space for reliable motion estimation. The artifact level in I_b is predicted using the maximum angle between two radial profiles (α), similar to (25). To guarantee that the image quality of I_b is sufficient for reliable motion estimation we perform an adaptive binning that forces each bin to have α_b (maximum angle between two radial profiles in bin b) smaller than a predetermined α_{max} (determined empirically). To minimize intra-bin motion, only bins with a bin window (w_b) smaller than a maximum bin window (w_{max}) are accepted.

Here, we perform an adaptive binning (Figs. 1d,e) with constraints to ensure reliable motion estimation. This process is controlled by 4 parameters: maximum overall undersampling factor (R_{max}), the maximum angle (α_{max}), the maximum bin window size (w_{max}) and the minimum
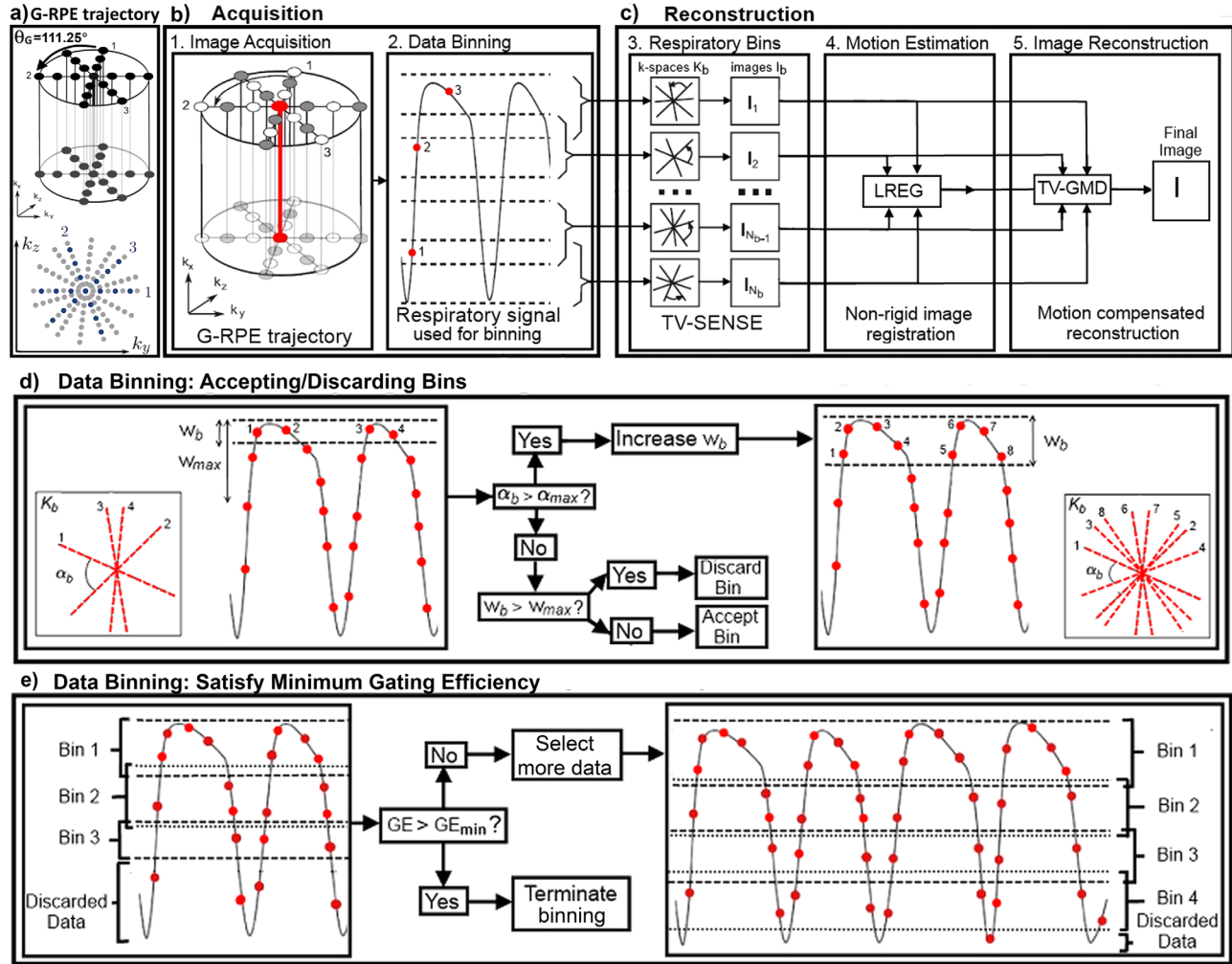
FIG. 1. **a**: Top: Diagram of the golden radial phase encoding (GRPE) trajectory. Cartesian readouts (k_x direction) are acquired with a radial order in the phase encoding plane ($k_y - k_z$). Consecutive radial profiles (numbered 1, 2, and 3) are separated by the golden angle $\theta_G = 111.25°$. a: Bottom: Diagram of GRPE undersampling in the phase encoding plane. Angular undersampling is achieved by skipping complete radial profiles (full gray radial profiles), while radial undersampling is performed along each radial profile by uniformly skipping readouts (gray readouts along radial profiles 1, 2, and 3). **b,c**: Diagram of the proposed approach in five steps. The acquisition is comprised of two parts: step 1. Image is acquired with 3D G-RPE; step 2. The central k-space line yields a respiratory signal which is used to bin data. The reconstruction is divided into 3 parts: step 3. Binned datasets are simultaneously reconstructed with TV-SENSE; step 4. Motion is estimated by image registration (LREG) of the binned reconstructions; step 5. The estimated motion is used in the motion compensated reconstruction. Only the acquired data are needed to produce a motion compensated image. Adaptive data binning is performed in two steps: **d**: Each bin is initialized with a window size w_b. If α_b is larger than α_{max}, w_b is increased, providing additional data for this bin. This process is repeated until α_{max} is respected. If the final w_b is larger than w_{max}, the bin is discarded; otherwise it is accepted. **e**: Insufficient data cause a significant fraction of bins to be discarded, leading to a poor gating efficiency (*GE*). If *GE* is smaller than GE_{min}, an additional radial profile is considered and the full dataset (including the newly considered radial profile) is re-binned. This process terminates when the GE_{min}, α_{max} and w_{max} constraints are simultaneously respected.

gating efficiency (GE_{min}). Gating efficiency (*GE*) is given by:

$$GE = \frac{Accepted\ Profiles}{Total\ Profiles\ Acquired} \qquad [1]$$

Respiratory bins are chosen such that within each bin, $\alpha_b < \alpha_{max}$ (to limit reconstruction artifacts), and $w_b < w_{max}$ (to limit intra-bin motion). To limit undersampling artifacts in the final reconstruction of the complete dataset, a minimum amount of data to respect R_{max} is enforced. A potential bin is first generated at the end-exhale position with a bin window size equal to the image resolution. The bin window is increased until it has enough data to comply with the α_{max} constraint (Fig. 1d). If the bin window size exceeds w_{max} the bin is discarded to minimize intra bin motion, otherwise it is accepted. A sliding window is used to initialize a potential bin in the next respiratory position and the process in Figure 1d is repeated.

Once the considered data thus far have been binned, the algorithm tests if the selected dataset satisfies the minimum gating efficiency. If the current gating efficiency is less than GE_{min} (Fig. 1e), then an additional radial profile is considered and the binning process is

restarted (back to Figure 1d). Data binning terminates once enough motion states are adequately populated ($\alpha_b < \alpha_{\max}$, $w_b < w_{max}$) and the complete dataset satisfies the condition $GE > GE_{\min}$.

Reconstruction of Respiratory Bins

The undersampled bins are simultaneously reconstructed with total variation regularized iterative SENSE (TV-SENSE) (26,27) given by:

$$\hat{I}_b = \ arg \ min_{I_b}\{||EI_b - K_b||_2^2 + \lambda_s TV_s + \lambda_t TV_t\} \quad [2]$$

where K_b is the acquired data at each bin b, E is the encoding matrix including coil sensitivities, gridding and Fourier transformation, I_b the binned images to be reconstructed, TV_s represents the 3D spatial total variation (intra-bin) and TV_t the temporal total variation in the respiratory direction (inter-bin). The l_2-norm is the data consistency term. TV_s is the sum of absolute differences in each bin; TV_t is the sum of absolute differences between adjacent bins. Both of these transforms are l_1-norms operating in image space, defined as:

$$TV_s = ||\nabla_s I_b||_1 \quad [3]$$

$$TV_t = ||\nabla_t I_b||_1 \quad [4]$$

where ∇_s and ∇_t represent the 3D spatial gradient and the 1D temporal gradient, respectively. The parameters λ_s and λ_t define the balance between total variation regularization and data consistency. The TV_s term removes noise-like aliasing in the image and sharpens the main edges in the image, e.g., the diaphragm–lung boundary, allowing better image registration. Large λ_s values enhance these effects at the expense of additional blurring (due to over-smoothing). While blurring limits the accuracy of subsequent image registration, aliasing introduces errors in I_b that can make the registration fail altogether. Hence, we use a large value for λ_s to reconstruct artifact-free respiratory bins and allow reliable motion estimation. The TV_t removes additional aliasing in areas where there is little motion, like the central part of the liver. Large λ_t values will introduce blurring in regions with large motion, e.g., diaphragm–lung boundary. Thus, we use small λ_t values to distinguish motion states. Here, the TV_t term amounts to a small regularization compared with TV_s, yielding minor improvements in the reconstructed image. The values for λ_s and λ_t were determined empirically by inspecting the output reconstructions of four training datasets covering the expected range of undersampling factors and respiratory amplitudes and choosing values that removed the most background aliasing without significantly blurring the image.

To accelerate bin reconstruction, a data consistency reconstruction (i.e. λ_s and λ_t set to zero) is used as the starting estimate for TV-SENSE. This approach accelerates convergence and delivers a good approximation of the reconstructed image. These reconstructions are preconditioned (23) by intensity correction (from coil sensitivities) and a Voronoi based density compensation function (28), as our data acquisition (G-RPE) is non-Cartesian.

Motion Estimation

A 3D nonrigid respiratory motion model is obtained from image registration of reconstructed bin images to a common respiratory position. This is done using the LREG tool (29), which performs an intensity based registration through a succession of local affine registrations, starting from a global affine down to small image blocks. The resulting deformation field is thus nonrigid.

Image Reconstruction

The final undersampled image is reconstructed using a spatial total variation regularized GMD approach, based on the formalism introduced in Batchelor et al (13). The GMD approach is described by:

$$K = \sum_b A_b F S_c U_b I = EI \quad [5]$$

where I is the ideal (motionless) image, U_b are the spatial transformations for bin b obtained with LREG, S_c are the coil sensitivities for coil c, F is the forward Fourier transform, A_b is a logical matrix that selects the k-space lines acquired for bin b, and K is the acquired multichannel k-space data. Equation [5] is in the reference frame of the coils, where they are assumed to remain static. I may be obtained by inverting the encoding operator E. Practical inversion of E is obtained with iterative methods such as the conjugate gradient (CG). The CG requires a symmetric positive-definite matrix, thus we apply the method to the equivalent normal equation:

$$E^H K = (E^H E)I \quad [6]$$

where E^H is the Hermitian transpose of E.

The proposed approach uses undersampled data, which results in noise amplification in the reconstructed motion corrected images due to poor conditioning of the inversion. This happens for two reasons: first, if the object moves outside the field-of-view (FOV) then information is permanently lost; second, correcting for motion within the FOV may cause k-space inconsistencies, causing some samples to overlap and creating k-space gaps. This effectively increases the undersampling factor (R), which contributes to making Eq. [6] undetermined (30). Furthermore, in practice the motion is not known exactly and errors in motion estimation can further contribute to the poor conditioning of this problem. It has been shown how multiple channels improve the condition of the motion reconstruction problem for fully sampled images (30). To reduce the effect of poor conditioning in undersampled datasets we include spatial total variation regularization TV_s in the GMD reconstruction (TV-GMD), given by:

$$\hat{I} = arg \ min_I\{||EI - K||_2^2 + \lambda_s TV_s\} \quad [7]$$

This is solved with a nonlinear conjugate gradient reconstruction using the solution to the nonregularized approach as a starting estimate, similar to the previous

description of the bin reconstruction. In the TV-GMD reconstruction, the TV_s term is used to remove noise-like aliasing with small λ_s values. The λ_s for the TV-GMD was determined empirically by choosing a value that reduces the remaining artifacts without significantly affecting image sharpness.

Data Acquisition

Nine healthy volunteers were scanned under free-breathing on a 1.5 Tesla (T) clinical scanner (Philips Achieva, Philips Healthcare, Best, The Netherlands) using a 32-channel cardiac coil. Written informed consent was obtained according to institutional guidelines. Data were acquired with a balanced steady state free precession sequence with the following parameters: 287 × 287 × 287 mm isotropic FOV, 1.75 × 1.75 × 1.75 mm isotropic resolution, (TR/TE) = 3/1.43 ms, flip angle 30°. During acquisition, each radial profile was uniformly undersampled in the radial direction by a factor of 2. For the resulting reconstructed matrix size of 164 × 164 × 164, we need 256 radial profiles to approximately fulfil the Nyquist criterion in the angular direction, assuming a quasi-uniform profile distribution. During the scan, 820 radial profiles were acquired to guarantee all volunteers provided enough data for different reconstruction approaches, including the self-gated reconstruction which has a low scan efficiency.

Simulations

The proposed approach estimates motion from highly undersampled respiratory resolved bin reconstructions (I_b). A pseudo-random distribution of radial profiles is sampled at each respiratory bin, depending on the breathing pattern. This may result in large k-space gaps that can introduce artifacts in the reconstructed images. Specifically, k-space gaps affect the image point spread function by broadening the main lobe/increasing side lobe amplitude, which results in blurring/aliasing artifacts (24). Blurring and residual artifacts may hinder subsequent image registration, producing inaccurate motion fields. A simulation was conducted in one representative volunteer to study the relationship between the maximum angle between two radial profiles (α_{max}) and the accuracy of motion estimation. An end-inhale image (F) was reconstructed with 25 different numbers of radial profiles (p), from fully sampled (256 profiles) to highly undersampled (26 profiles). The obtained undersampled images (F_p) were registered to a reference fully sampled end-exhale image (F_r). The obtained motion fields were then compared with the ground-truth: the registration between F_r and F. We measure the average displacement error in the motion field $\varepsilon(\alpha)$ similar to (25):

$$\varepsilon(\alpha) = \frac{\sum_1^N \sqrt{\left(\overrightarrow{U}_{\alpha(Kp)}(n) - \overrightarrow{U}_{Fr}(n)\right)^2}}{N} \qquad [8]$$

where $U_{\alpha(Kp)}$ is the motion field between F_p and F_r, U_{Fr} is the motion field between F and F_r, and the sum is taken over all the voxels (N being the total number of voxels in the image).

Comparison with Image Based Motion Compensation

A preliminary study was performed to compare the approach described in Buerger et al (16), hereby referred as image-based motion compensation (IMC) with the proposed TV-GMD. To evaluate the effects of blurring and residual artifacts in motion estimation, bin reconstructions using the α_{max} value, obtained by means of simulations, were performed using iterative SENSE (as in IMC) and with the proposed TV-SENSE. Motion fields between neighboring bins of representative volunteers were obtained by means of LREG. A comparison of motion estimation obtained from undersampled SENSE and TV-SENSE bin reconstructions was made by computing their displacement errors to motion fields obtained from a dataset 3× oversampled in the angular direction (considered as ground truth). Additionally, all nine datasets were reconstructed with IMC, using the same amount of data as the TV-GMD reconstruction. This resulted in a total of 160 ± 37 acquired profiles for both TV-GMD and IMC reconstructions. IMC reconstruction was performed with iterative SENSE (23), taking approximately 1 h. IMC and TV-GMD reconstructions were compared by means of measures of liver sharpness and gradient entropy. TV-GMD reconstruction and the comparison metrics are described in more detail in the following section.

In Vivo Experiments

The same acquired data were used retrospectively to produce a 2× undersampled non-motion corrected (NMC) reconstruction (2× undersampling in radial direction, no undersampling in angular direction), a 2× undersampled 5 mm self-gated reconstruction (2× undersampling in radial direction, no undersampling in angular direction), and a highly undersampled TV-GMD reconstruction (2× undersampling in radial direction, 1.8× undersampling in angular direction, on average). This resulted in a total of 256, 414 ± 147 and 160 ± 37 acquired profiles for the NMC, gated and TV-GMD reconstructions.

The following binning parameters were used: $\alpha_{max} = 13.75°$ (determined according to the previous section); $w_{max} = 5$ mm (same value as the gating window); $GE_{min} = 80\%$ (set to remove outliers in the respiratory cycle). Furthermore, to avoid remaining undersampling artifacts in the final motion corrected reconstruction a maximum undersampling factor (R_{max}) of 4 was used. Therefore, the proposed method was set to reconstruct a minimum of 128 radial profiles, equivalent to 2× angular undersampling and 2× radial undersampling. This resulted in data being grouped into three to five bins (varying per volunteer), with bin undersampling factors ranging from 5.2× to 18.9× (average of 9.5×). The motion corrected datasets were undersampled from a minimum of 2.1× to a maximum of 4× (average of 3.6×). Table 1 presents values for undersampling factors, gating efficiency, acquisition time, number of acquired profiles, number of profiles per bin, number of bins, and bin window sizes. The respiratory bins were reconstructed with TV-SENSE. The initial l_2-norm reconstruction ran with 10 iterations, with $\lambda_s = 0$ and $\lambda_t = 0$. This result was used as a starting estimate for the reconstruction with $\lambda_s = 0.2$

Table 1
Acquisition and reconstruction information for non-motion corrected (NMC), gated, GMD and TV-GMD reconstructions.

Acquisition and reconstruction	NMC	Gated	GMD	TV-GMD
Number of bins	1	1	3-5	3-5
Gating/Bin windows (mm)	11.1 ± 3.5	5.00	2.76 ± 1.1	2.76 ± 1.1
Number of profiles per bin	256	256	49 ± 16	49 ± 16
Number of profiles acquired	256	414 ± 147	160 ± 37	160 ± 37
Number of profiles reconstructed	256	256	148 ± 37	147 ± 37
Acquisition time (s)	62.98	101.79 ± 36.21	39.36 ± 9.13	39.36 ± 9.13
Gating efficiency (%)	100	67 ± 15	93 ± 7	93 ± 7
Undersampling factor	2	2	3.6 ± 0.5	3.6 ± 0.5

and $\lambda_t = 0.1$ (corresponding to 9.6×10^{-6} and 4.8×10^{-6}, respectively, in terms of the average $||.||_\infty$ norm of the images), three iterations. The reconstructed bins were registered to estimate the motion for the TV-GMD reconstruction. The initial data consistency GMD reconstruction ran with five iterations, $\lambda_s = 0$. The following TV-GMD reconstruction used $\lambda_s = 0.0001$ (corresponding to 4.8×10^{-9}, in terms of the average $||.||_\infty$ norm of the images) and five iterations. Additionally, data were reconstructed with GMD (4 iterations) for additional comparison with TV-GMD. It took approximately 1.5 h to reconstruct bins (TV-SENSE) and an additional 1.5 h for the motion compensated reconstruction (TV-GMD) on a 12-core implementation. The gated and nonmotion corrected images were reconstructed with iterative SENSE (23), both taking approximately 5 min to reconstruct. Coil sensitivities were estimated from a reference scan. All images were reconstructed using Matlab (The Math-Works, Natick, MA).

To observe the effect of undersampling in the final motion corrected reconstruction, data from two representative volunteers were reconstructed with the proposed method with undersampling factors of 4×, 3×, 2×, and 1×, using the same estimated motion as described above.

The proposed TV-GMD approach was compared with the gated reconstruction by means of liver sharpness, gradient entropy, visual image scoring and ranking (31). The liver sharpness and gradient entropy metrics were computed on a set of 10 coronal slices. To compute liver sharpness, twenty-five 1D profiles were manually selected across the liver–lung interface. The sharpness measure for each profile was obtained by the maximum gradient normalized to the maximum intensity, similar to Botnar et al (32). Gradient entropy has previously been used in motion correction as an optimization cost function that favors distinct boundaries and reduced artifacts and was ranked 1 of 24 image quality metrics studied (33). Here we use local gradient entropy as an image quality metric, similar to Vuissoz et al (34). The total gradient entropy of the image is given by the mean of the local gradient entropies. All liver sharpness and gradient entropy values were normalized to the reference gated values. We present the gradient entropy results inverted to allow easier comparison with the other metrics (the higher the metric the better the image). Two experts (a radiologist with 14 years of experience in MRI and an image processing researcher with 18 years of experience in MRI) were asked to "score the sharpness of the main boundaries and features of the images" on a scale of 0 (extreme blurring) to 4 (no blurring) and "rank the overall image quality based on existing artifacts, ghosting and blurring" from 1 (worst) to 4 (best). Statistical significance of gradient entropy and liver sharpness was evaluated using a paired t-test (P-value of 1%); statistical significance of expert sharpness score and quality rank was evaluated using a Wilcoxon signed rank test (P-value of 1%).
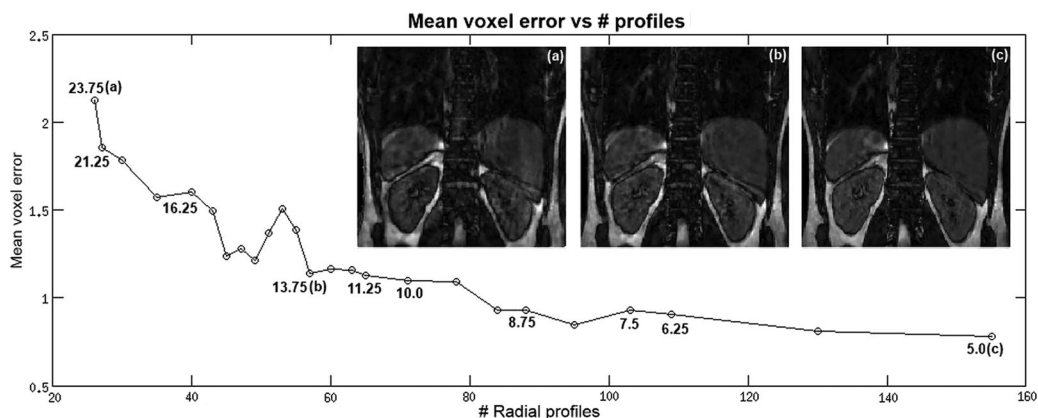

FIG. 2. Plot of the mean motion field error as a function of the number of radial profiles used for bin reconstruction. Several α values are marked in the graph. Respiratory bin reconstruction for the volunteer studied for 3 different α values are shown: **(a)** $\alpha = 5°$, **(b)** $\alpha = 13.75°$, and **(c)** $\alpha = 16.25°$. For $\alpha \leq 13.75°$, motion field errors are kept below 1.1 voxels.
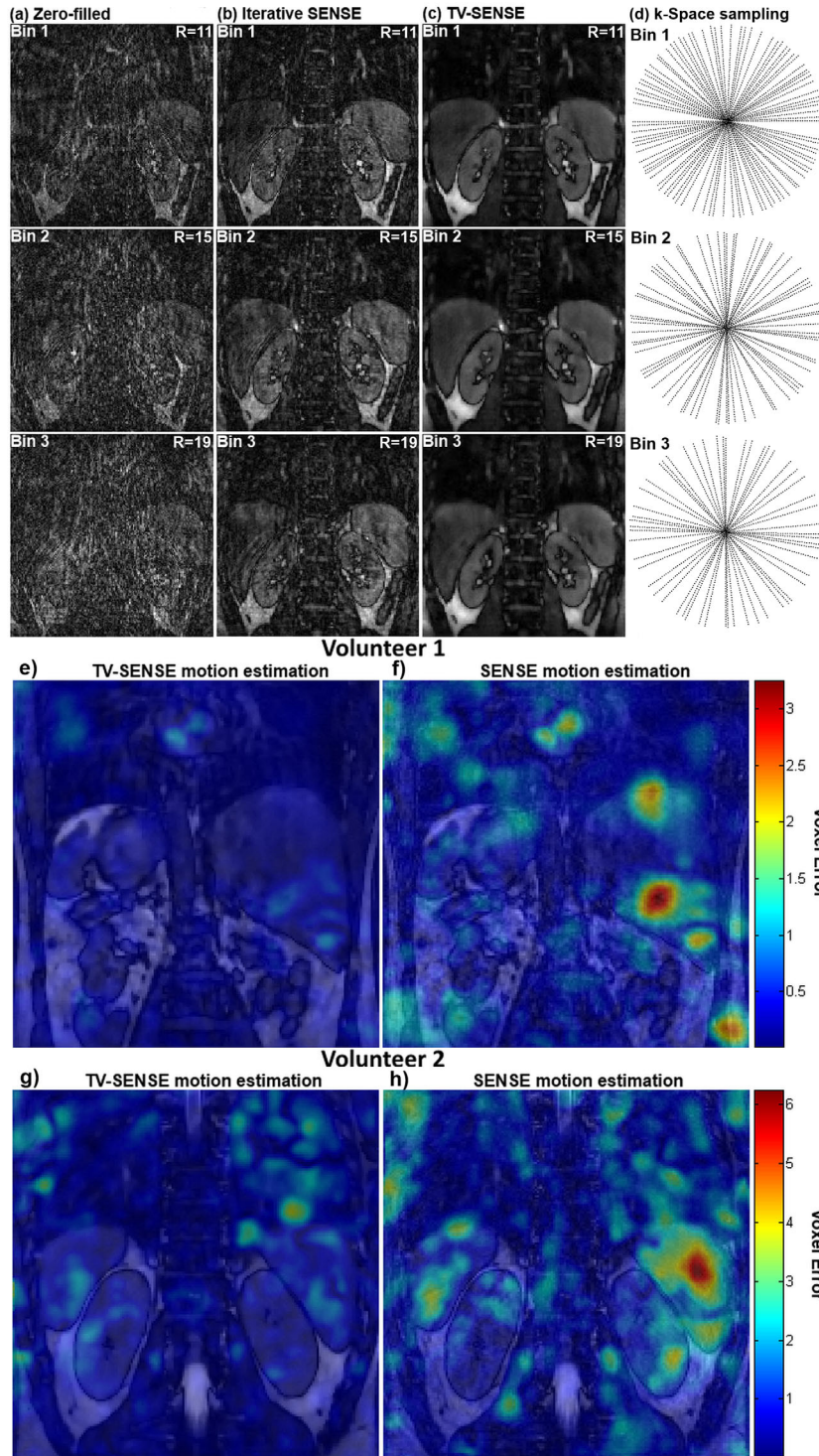
FIG. 3. Reconstructions of bins 1, 2, and 3 with 46, 33 and 27 radial profiles (corresponding to undersampling factors R of 11, 15 and 19, respectively). **a**: Zero-filled reconstructions. **b**: Iterative SENSE used in (16), significant aliasing remains. **c**: TV-SENSE, most aliasing is eliminated. **d**: k-Space sampling locations in the phase encoding plane for bins 1, 2, and 3. **e–h**: Motion estimation errors (in voxel units) between neighboring bins for TV-SENSE and iterative SENSE bin reconstructions for two volunteers. Color coded motion estimation errors are overlaid on the anatomical reconstruction. Iterative SENSE motion estimation (f–h) shows increased local errors, whereas TV-SENSE provides more reliable motion estimation (e–g).

RESULTS

Simulations

Figure 2 shows the mean voxel error in the registration deformation field decreasing with the increasing number of radial profiles. Angular gaps values (α) resulting for different number of radial profiles are displayed throughout the graph. For values lower than $\alpha = 13.75°$ the mean voxel error in the motion fields remains below 1.1 voxels. For α values larger than $13.75°$ the error in the motion fields start increasing significantly. Based on this simulation, we chose to set $\alpha_{max} = 13.75°$.

Comparison with Image Based Motion Compensation

Figures 3a–c show bin images of volunteer 2 for a zero-filled reconstruction, iterative SENSE and TV-SENSE for resulting undersampling factors (R) of $\approx 11\times$, $\approx 15\times$, and
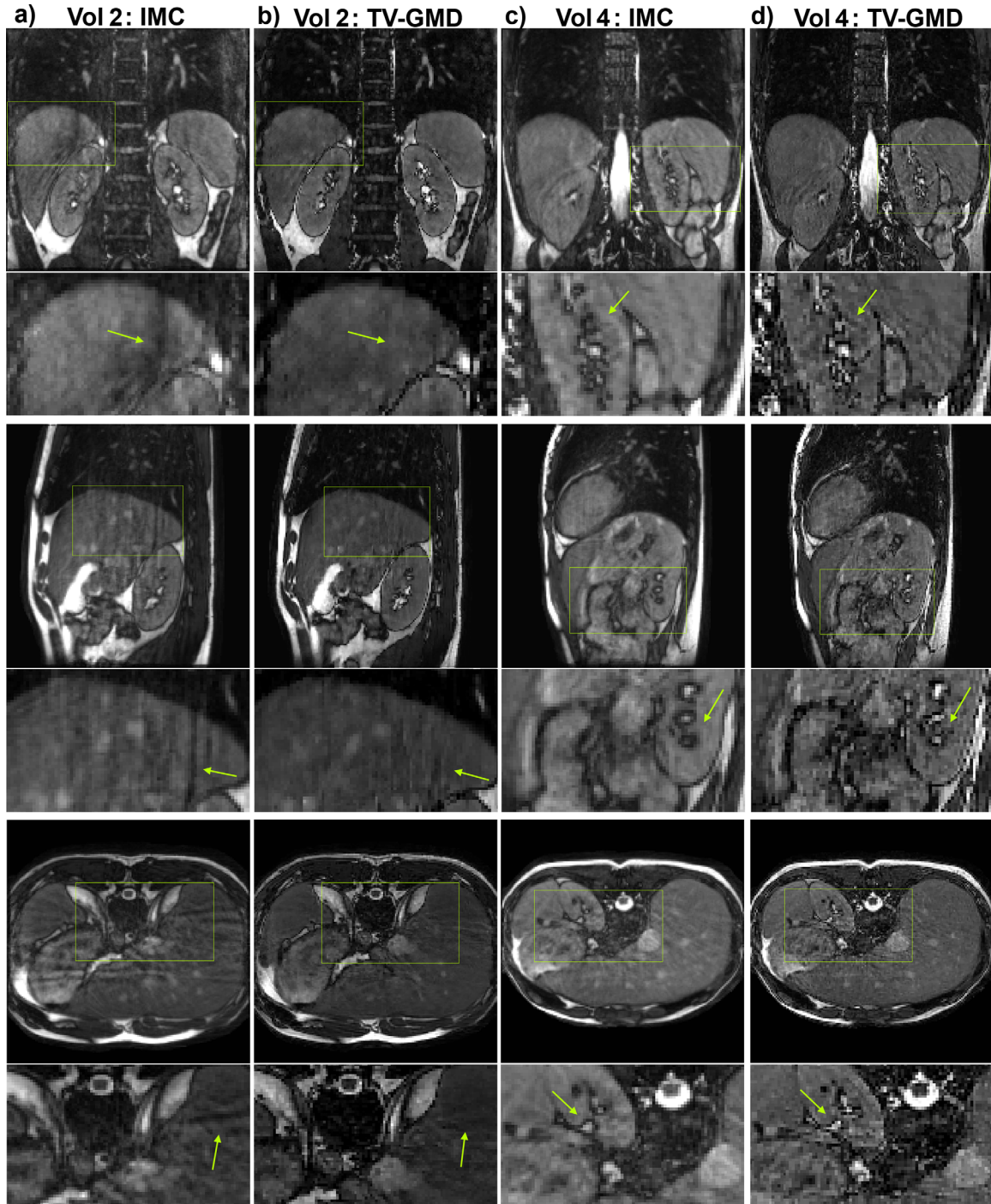
FIG. 4. Coronal (top), sagittal (middle) and axial (bottom) slices for volunteers 2 and 4 (including zoom-in images, arrows point out some main differences). **a**: Image based motion correction (IMC) for volunteer 2 with 4× undersampling at 100% gating efficiency. Residual aliasing may be seen in all slice orientations. Additionally, some blurring is introduced by IMC. **b**: Proposed TV-GMD for volunteer 2 with 4× undersampling at 100% gating efficiency. Residual aliasing is reduced and image structures appear sharper when compared with IMC. **c**: IMC for volunteer 4 with 4× undersampling at 100% gating efficiency. Residual aliasing is not significant in this volunteer, but the IMC still introduces additional blurring to the image. **d**: TV-GMD for volunteer 4 with 4× undersampling at 100% gating efficiency. A sharper reconstruction is obtained with the TV-GMD.

≈19× for bins 1, 2, and 3, respectively. Iterative SENSE reconstruction, as used in Buerger et al (16), shows residual artifacts (Fig. 3b). These artifacts are significantly reduced with a TV-SENSE reconstruction, while only introducing minor blurring (Fig. 3c).

The improvement in motion estimation accuracy with the proposed TV-SENSE in comparison to previously shown iterative SENSE can be seen in Figures 3e–h, for two representative volunteers. Image registration of SENSE reconstructions can produce local errors
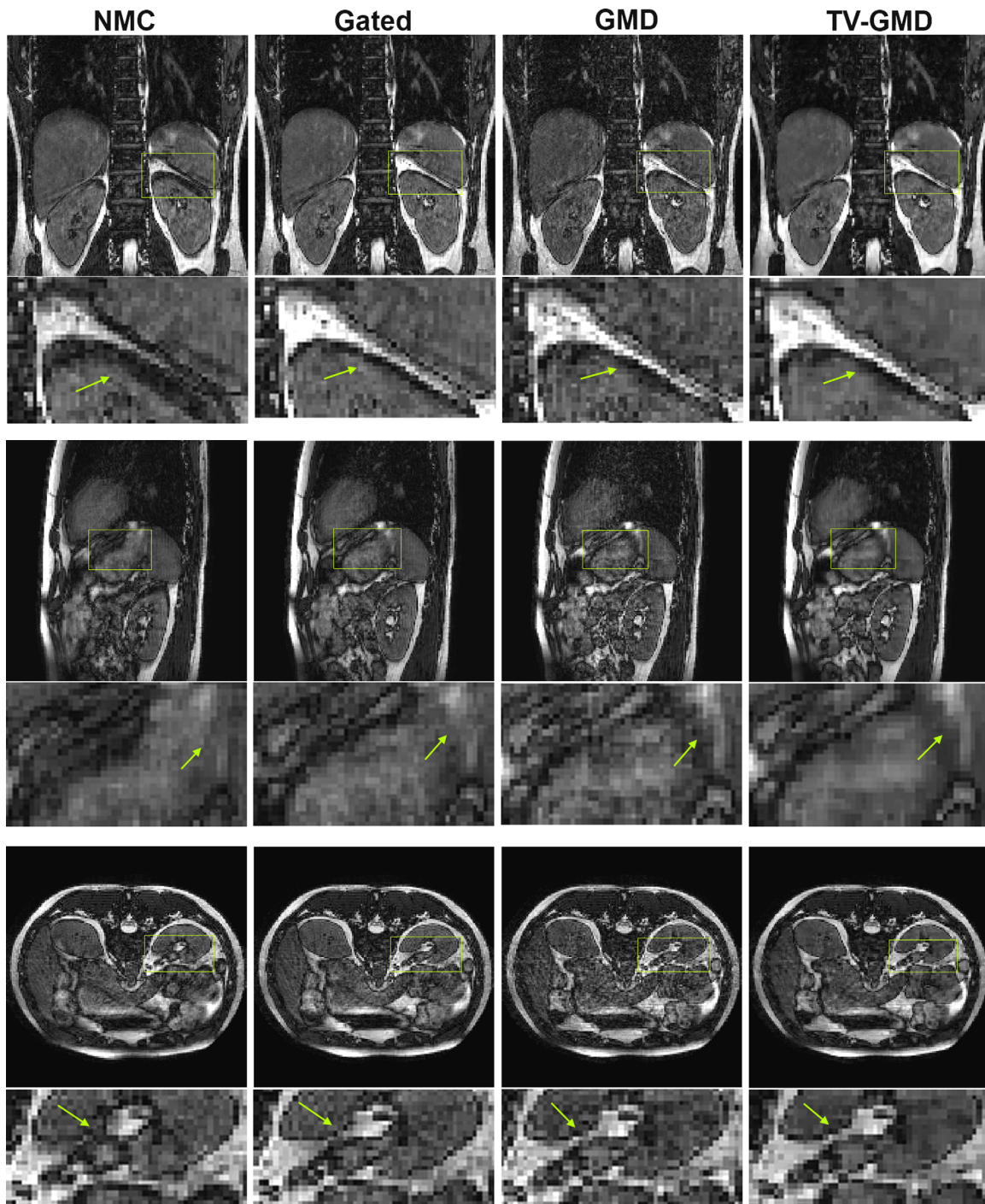
FIG. 5. Coronal (top), sagittal (middle) and axial (bottom) slices for volunteer 1 with maximum respiratory amplitude of 14.8 mm (including zoom-in images, arrows point out some main differences). **NMC (non-motion corrected):** 2× undersampled at 100% gating efficiency. Several structures in the image are corrupted by motion. **Gated:** 2× undersampled at 60% gating efficiency. Most structures are sharper than the NMC. **GMD:** 3.5× undersampled at 80% gating efficiency. The GMD is sharper than the NMC, but presents remaining undersampling artifacts. **TV-GMD:** 3.5× undersampled at 80% gating efficiency. The total variation regularization improves undersampled reconstruction at the expense of minor blurring.

(yellow-red regions in Figures 3f,h) as the LREG algorithm attempts to register aliasing artifacts. TV-SENSE removes most of these artifacts, enabling reliable motion estimation (corresponding blue-green regions in Figures 3e,g).

Figure 4 shows multiple slice orientations of two volunteers for image-based motion compensation (IMC) and TV-GMD reconstructions. If undersampling artifacts from different motion states fail to cancel out, residual aliasing may arise in IMC as shown in Figure 4a for volunteer 2.
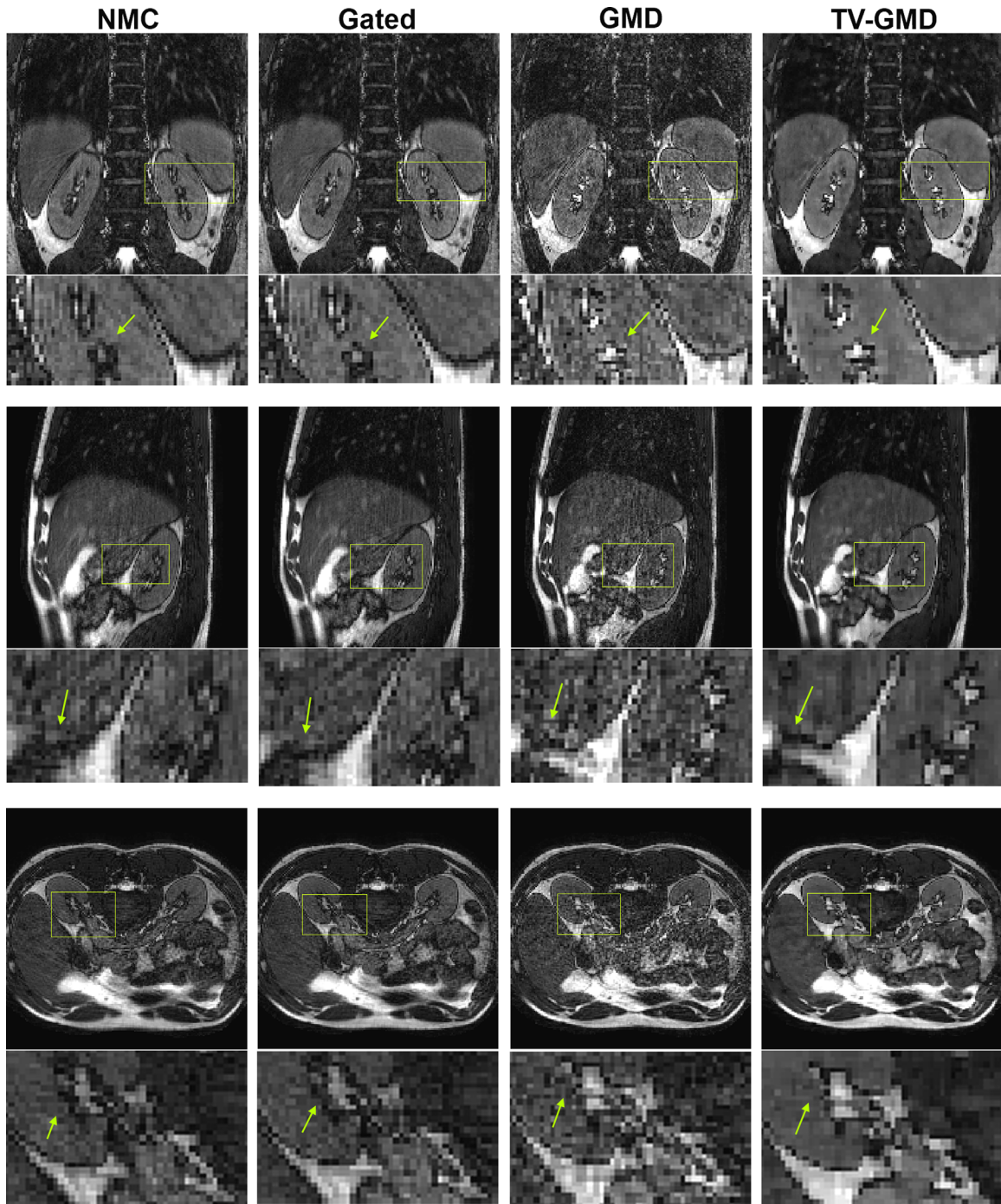
FIG. 6. Coronal (top), sagittal (middle) and axial (bottom) slices for volunteer 2 with maximum respiratory amplitude of 8.2 mm (including zoom-in images, arrows point out some main differences). **NMC (non-motion corrected):** $2\times$ undersampled at 100% gating efficiency. Some blurring is visible in image structures and the liver–lung border. **Gated:** $2\times$ undersampled at 77% gating efficiency. There is no significant improvement, as the gated reconstruction uses a 5 mm window. **GMD:** $4\times$ undersampled at 96% gating efficiency. The high undersampling creates a strong noise-like aliasing. **TV-GMD:** $4\times$ undersampled at 96% gating efficiency. The total variation regularization improves GMD undersampled reconstruction at the expense of some minor blurring, despite using only 128 radial profiles.

This aliasing is significantly reduced with the TV-GMD (Fig. 4b). Results for volunteer 4 using IMC (Fig. 4c) present less residual aliasing, but additional blurring is introduced (which can be seen in both volunteers). In contrast, the TV-GMD corrects motion without introducing this additional blurring (Fig. 4d). TV-GMD and IMC presented liver sharpness values of 1.18 and 0.98, respectively, and gradient entropy values of 1.00 and 0.98, both statistically different with a *P*-value of 1%.
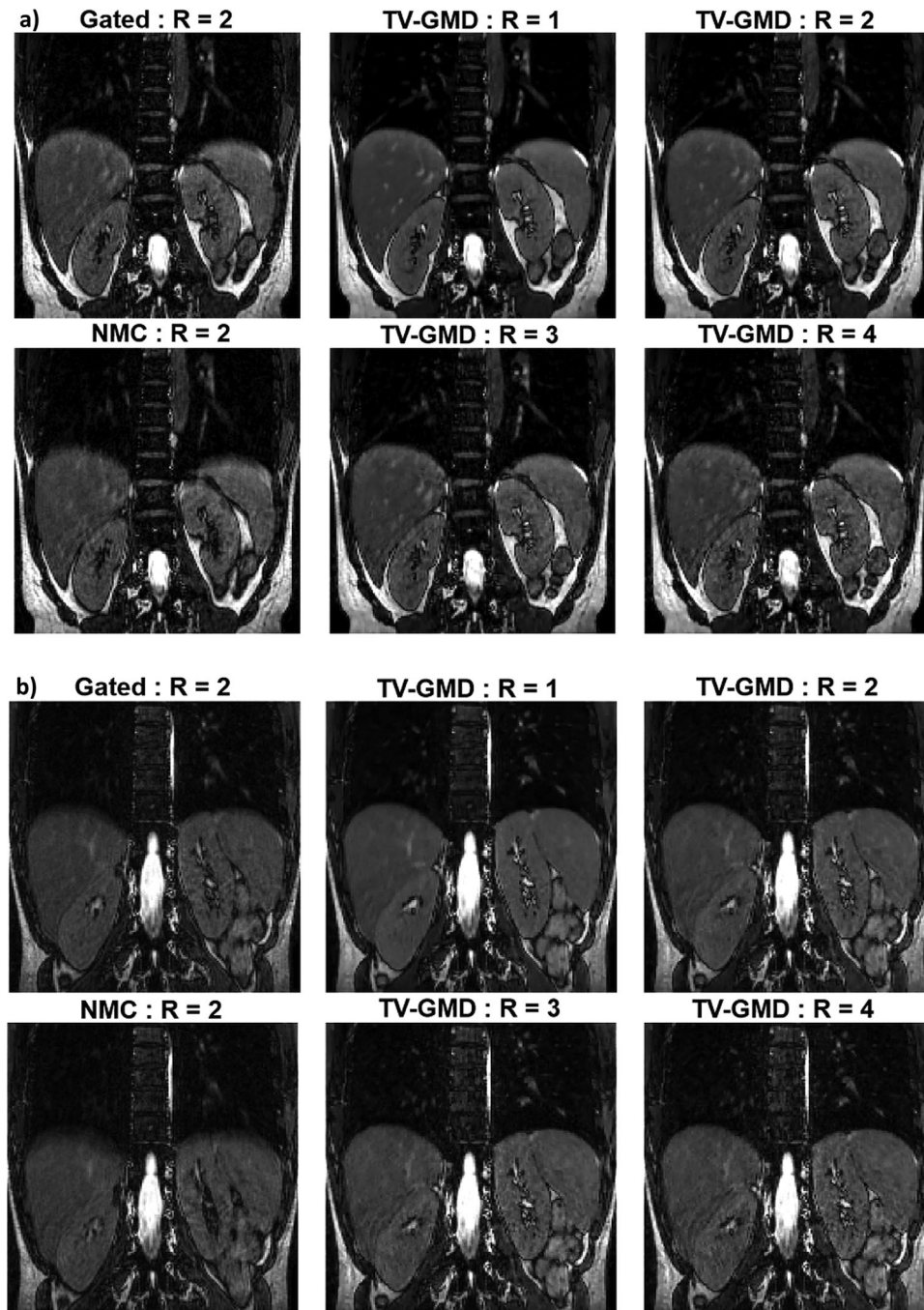
FIG. 7. **a**: Coronal slices for volunteer 3 reconstructed with TV-GMD at undersampling factors (R) of 4×, 3×, 2×, and 1×, corresponding to 128, 170, 256, and 512 radial profiles, respectively. The gated and nonmotion corrected (NMC) reconstructions have an undersampling factor of 2. A signal-to-noise improvement is visible as more data are used for the reconstruction. Vessel features benefit particularly from this additional data. **b**: Coronal slices for volunteer 4 reconstructed with TV-GMD at undersampling factors (R) of 4×, 3×, 2×, and 1×, corresponding to 128, 170, 256, and 512 radial profiles, respectively. The gated and non-motion corrected (NMC) reconstructions have an undersampling factor of 2. Small, low contrast features in the image become better defined with the TV-GMD reconstruction and benefit from the lower undersampling factors.

In Vivo Experiments

Figure 5 shows multiple slice orientations for the non-motion corrected, gated, GMD and TV-GMD reconstructions for volunteer 1. In Figure 5, it can be seen that TV-GMD and gated reconstructions yield images of similar quality, correcting most ghosting and blurring present in the non-motion corrected (NMC). The gated and NMC reconstructions have an undersampling factor of 2×, while the GMD and TV-GMD resulted in an undersampling of 3.5× for this volunteer. Remaining artifacts from undersampling and noise amplification can be observed in the GMD reconstruction (Fig. 5). This effect is consistent across all volunteers and increases for higher undersampling factors. Comparison between GMD and TV-GMD highlights how TV regularization improves the conditioning of the reconstruction. Figure 6 shows multiple slice orientations for volunteer 2, where the GMD and TV-GMD reconstructions resulted in an undersampling of 4×, compared with 2× for the gated and NMC. The TV-GMD presents a sharper reconstruction than the gated (Fig. 6), due to the fact that the resulting binning windows were smaller (2.76 mm average) than the gating window (5 mm). Note that undersampling artifacts are stronger for this case, but still can be reduced by TV regularization.
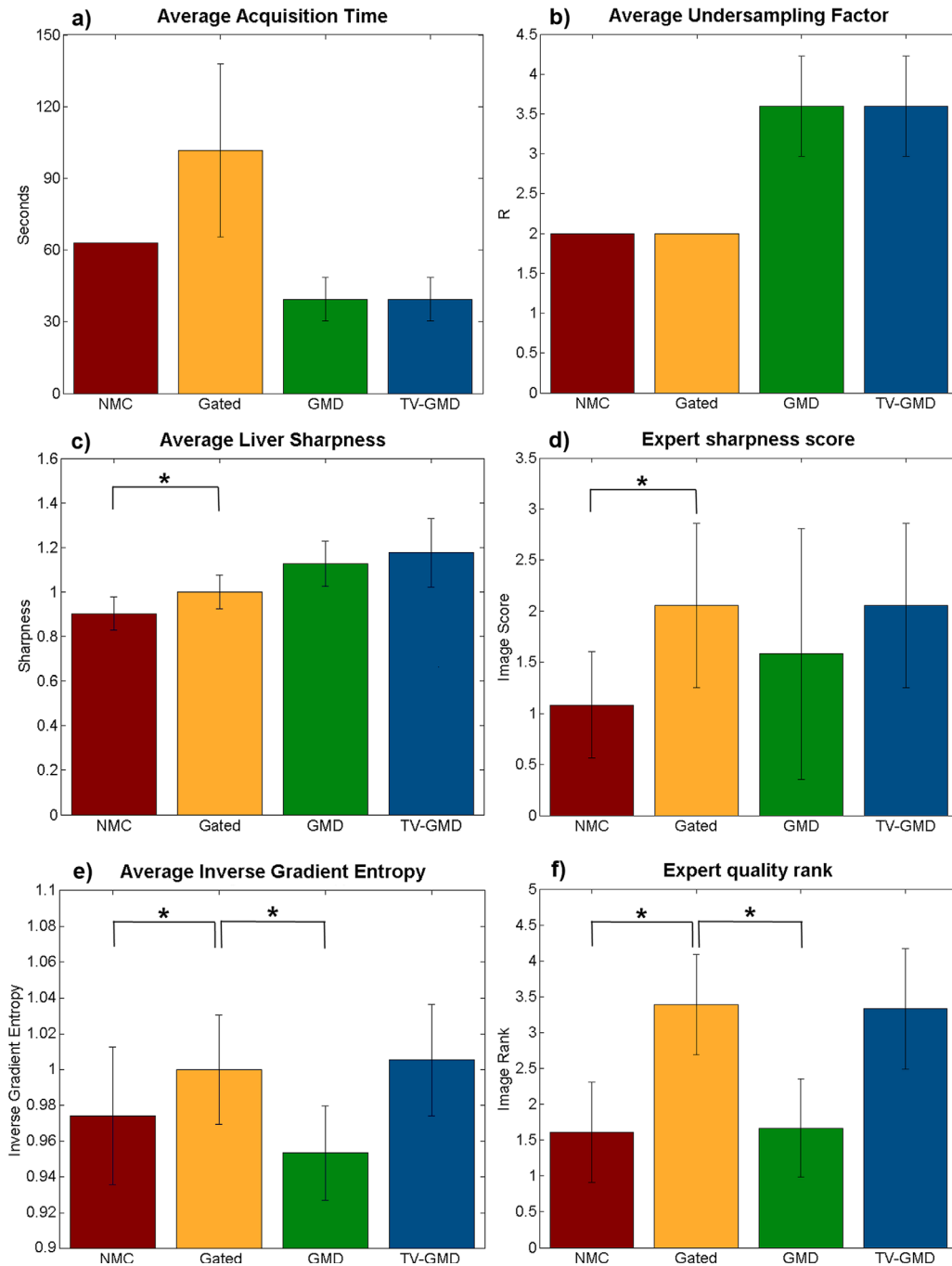
FIG. 8. Bar plots comparing the performance of the non-motion corrected (NMC), gated, GMD and proposed TV-GMD reconstructions in terms of average acquisition time **(a)**, average undersampling factor **(b)**, average liver sharpness **(c)**, expert sharpness score (0: extreme blurring to 4: no blurring) **(d)**, average (inverse) gradient entropy **(e)**, and expert overall quality rank (1: worst to 4: best) **(f)**. Statistically different results with a *P*-value of 1% are marked with (*).

Reconstructions for the TV-GMD at various undersampling factors in two volunteers are shown in Figures 7a,b. As expected, undersampling artifacts decrease with increasing data used. The proposed method is flexible in the choice of the maximum undersampling factor of the reconstructed image which may be useful for clinical applications that require specific signal-to-noise ratios.

Bar plots of the average acquisition times, undersampling factors, gradient entropies, liver sharpness, sharpness score, and image quality rank over all nine volunteers are shown in Figure 8. When comparing with the gated reconstruction, the TV-GMD reconstruction reduces the average scan time from 101 to 34 s. The gradient entropy indicates the TV-GMD and gated reconstructions have the best image quality (1.00 and 1.00, respectively), significantly better than NMC (0.97) and GMD (0.95). Image rank from visual assessment agreed with gradient entropy, marking TV-GMD (3.33) just below the gated (3.39), significantly better than NMC (1.61) and GMD (1.67). Image sharpness score from
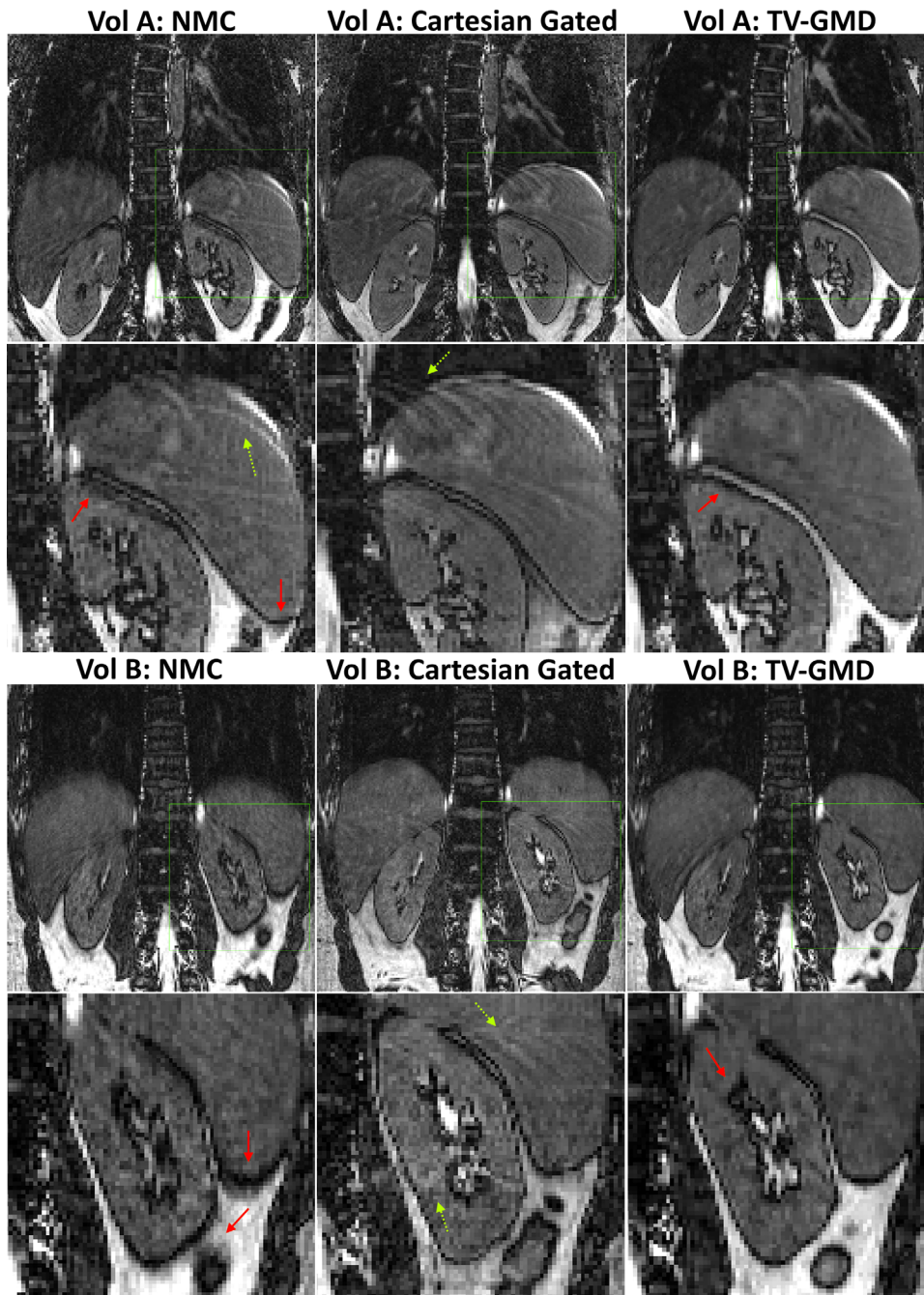
Vol A: NMC **Vol A: Cartesian Gated** **Vol A: TV-GMD**

FIG. 9. Coronal slices for a non-motion corrected (NMC) G-RPE 2× radially undersampled, Cartesian navigator gated (5 mm) 2× undersampled and TV-GMD G-RPE 2× radially undersampled for two volunteers. The Cartesian gated and TV-GMD approaches compensate motion to a comparable degree. Residual motion is still present in the Cartesian gated (ghosting, yellow dotted arrows) and TV-GMD (minor blurring, red full arrows).

Vol B: NMC **Vol B: Cartesian Gated** **Vol B: TV-GMD**

visual assessment yielded similar values between the TV-GMD (2.22) and gated (2.44), differentiating them from the NMC (1.17). Liver sharpness measures were not as sensitive as expert sharpness evaluation, but presented a similar behavior, marking TV-GMD as the best (1.18), followed by GMD (1.12) and gated (1.00), significantly better than NMC (0.90).

DISCUSSION

The proposed approach accelerates the acquisition by means of undersampling and 3D nonrigid motion correction, reducing the average scan time by 2.6× when compared with a gated acquisition. Here, motion is estimated (TV-SENSE) from highly undersampled respiratory resolved images and corrected in the reconstruction (TV-GMD) of the undersampled final data set. Gradient entropy and image quality ranking present similar values for the TV-GMD and gated reconstructions, distinguishing them as superior to the NMC and GMD. The noise-like aliasing present in the GMD reconstruction is responsible for the worse values in gradient entropy. The liver sharpness and expert sharpness score show the TV-GMD removes motion-induced blurring (visible in the NMC) to a similar level as the gated reconstruction. In cases of uniform breathing the TV-GMD achieves sharper

reconstructions than the gated as it uses binning windows (2.76 mm average) smaller than the gated window (5 mm).

This experiment was carried out retrospectively to compare different approaches, but the decision to stop a running acquisition once enough data have been acquired could be performed prospectively. This process requires a 1D FFT and a cross-correlation (to obtain the self-navigation signal), followed by the adaptive binning algorithm, taking less than 3 ms to compute. One limitation of the proposed method is the 3 hour reconstruction time. Reconstruction times increase with both the amount of data used and the number of bins. The bottleneck in these reconstructions is the nonuniform Fourier transform, which may be accelerated by GPU implementations (35). Another solution to this problem would be to use Cartesian trajectories with similar properties to the G-RPE, such as G-CASPR (12,36) or VDRad (37).

Note that the proposed approach requires a superior–inferior readout for self-navigation and alternative navigation strategies will be needed for trajectories with readouts in other directions. Another limitation is error propagation from motion estimation. If the estimated motion is not accurate, this can lead to artifacts in the TV-GMD reconstruction (results not shown here). Here we force every bin to respect α_{max} to guarantee accurate and reliable motion estimation. The proposed method is limited to inter-bin motion correction, thus a significant fraction of k-space remains uncorrected in the form of intra-bin motion. In this work, we perform motion compensated reconstructions with undersampling factors up to 4×. At high undersampling factors, over-regularization with total variation may create piecewise smoothing artifacts therefore an appropriate selection of a regularization parameter is needed.

It has been shown that GMD is capable of nearly perfect motion correction when the motion fields are known exactly (13). Thus, future improvements should target the motion estimation. First, self-navigation may be improved by using multiple coil information (38), as opposed to the single coil approach used here. Second, the number of bins may be increased by lowering the bin window size, w_{max}. This approach requires longer acquisitions and additional reconstruction time. However intra-bin motion and total variation artifacts of the motion corrected images should be reduced. Third, bin quality may be improved by introducing pseudo-random sampling in the radial direction, which may improve both motion estimation and motion compensated reconstruction. The value α_{max} was determined from a single volunteer study and although it provided successful reconstructions for all nine volunteers, further investigation may provide a more optimal setting.

A preliminary study was performed to compare the proposed approach with a Cartesian gated acquisition. 2× undersampled Cartesian navigator gated (5 mm) and G-RPE datasets were acquired on two healthy volunteers using the same parameters as before. Figure 9 shows coronal slices for a non-motion compensated (NMC) G-RPE 2× radially undersampled, Cartesian gated 2× undersampled (AP direction) and TV-GMD G-RPE 2× radially undersampled for two volunteers. These initial results show that Cartesian gated and TV-GMD remove most motion artifacts present in the NMC images. However, residual motion in the Cartesian gated creates coherent ghosting, whereas in TV-GMD it creates minor blurring. Further studies in patients will be needed for clinical validation.

CONCLUSIONS

A motion compensated reconstruction framework for accelerated 3D abdominal imaging has been presented. The proposed approach does not require additional training data or external sensors. Motion is estimated from highly undersampled data and incorporated into the reconstruction. In vivo results demonstrate the potential of the proposed method to provide similar image quality as a gated acquisition while reducing scan times by a factor of 2.6.

ACKNOWLEDGMENTS

REFERENCES

1. Wood M, Henkelman R. MR image artifacts from periodic motion. Med Phys 1985;12:143–151.
2. Ehman RL, McNamara MT, Pallack M, Hricak H, Higgins CB. Magnetic resonance imaging with respiratory gating: techniques and advantages. AJR Am J Roentgenol 1984;143:1175–1182.
3. Santelli C, Nezafat R, Goddu B, Manning WJ, Smink J, Kozerke S, Peters DC. Respiratory bellows revisited for motion compensation: preliminary experience for cardiovascular MR. Magn Reson Med 2011;65:1097–1102.
4. Scheffler K, Lehnhardt S. Principles and applications of balanced SSFP techniques. Eur Radiol 2003;13:2409–2418.
5. Welch EB, Rossman PJ, Felmlee JP, Manduca A. Self-navigated motion correction using moments of spatial projections in radial MRI. Magn Reson Med 2004;52:337–345.
6. Song R, Tipirneni A, Johnson P, Loeffler RB, Hillenbrand CM. Evaluation of respiratory liver and kidney movements for MRI navigator gating. J Magn Reson Imaging 2011;33:143–148.
7. Rohlfing T, Maurer C, O'Dell W, Zhong J. Modeling liver motion and deformation during the respiratory cycle using intensity-based free-form registration of gated MR images. Conf Proc SPIE Med Imaging 2001;4319:337–348.
8. Korin HW, Ehman RL, Riederer SJ, Felmle JP, Grimm RC. Respiratory kinematics of the upper abdominal organs: a quantitative study. Magn Reson Med 1992;23:172–178.
9. Forman C, Piccini D, Grimm R, Hutter J, Hornegger J, Zenge MO. Reduction of respiratory motion artifacts for free-breathing whole-heart coronary MRA by weighted iterative reconstruction. Magn Reson Med 2015;73:1885–1895.
10. Henningsson M, Prieto C, Chiribiri A, Vaillant G, Razavi R, Botnar RM. Whole-heart coronary MRA with 3D affine motion correction using 3D image-based navigation. Magn Reson Med 2014;71:173–181.
11. Pang J, Sharif B, Arsanjani R, Bi X, Fan Z, Yang Q, Li K, Berman DS, Li D. Accelerated whole-heart coronary MRA using motion-corrected

sensitivity encoding with three-dimensional projection reconstruction. Magn Reson Med 2015;73:284–291.

12. Prieto C, Doneva M, Usman M, Henningsson M, Greil G, Schaeffter T, Botnar RM. Highly efficient respiratory motion compensated free-breathing coronary mra using golden-step Cartesian acquisition. J Magn Reson Imaging 2014. doi: 10.1002/jmri.24602.

13. Batchelor PG, Atkinson D, Irarrazaval P, Hill DLG, Hajnal J, Larkman D. Matrix description of general motion correction applied to multi-shot images. Magn Reson Med 2005;54:1273–1280.

14. Cheng JY, Alley MT, Cunningham CH, Vasanawala SS, Pauly JM, Lustig M. Nonrigid motion correction in 3D using autofocusing with localized linear translations. Magn Reson Med 2012;68:1785–1797.

15. Atkinson D, Hill DLG, Stoyle PNR, Summers PE, Clare S, Bowtell R, Keevil SF. Automatic compensation of motion artifacts in MRI. Magn Reson Med 1999;41:163–170.

16. Buerger C, Prieto C, Schaeffter T. Highly efficient 3D motion compensated abdomen MRI from undersampled golden-RPE acquisitions. MAGMA 2013;26:419–429.

17. Cruz G, Atkinson D, Kolbitsch C, Schaeffter T, Prieto C. Comparison of non-rigid motion compensated reconstructions for 3D abdominal MRI. In Proceedings of the 22nd Annual Meeting of ISMRM, Milan, Italy, 2014. Abstract 4385.

18. Paschke N, Dossel O, Schaeffter T, Prieto C, Kolbitsch C. Comparison of image-based and reconstruction-based respiratory motion correction techniques for 3D whole-heart MRI. In Proceedings of the 22nd Annual Meeting of ISMRM, Milan, Italy, 2014. Abstract 5645.

19. White MJ, Hawkes DJ, Melbourne A, Collins DJ, Coolens C, Hawkins M, Leach MO, Atkinson D. Motion artifact correction in free-breathing abdominal MRI using overlapping partial samples to recover image deformations. Magn Reson Med 2009;62:440–449.

20. Odille F, Vuissoz P-A, Marie P-Y, Felblinger J. Generalized reconstruction by inversion of coupled systems (GRICS) applied to free-breathing MRI. Magn Reson Med 2008;60:146–157.

21. Prieto C, Uribe S, Razavi R, Atkinson D, Schaeffter T. 3D undersampled golden-radial phase encoding for DCE-MRA using inherently regularized iterative SENSE. Magn Reson Med 2010;64:514–526.

22. Boubertakh R, Prieto C, Batchelor PG, Uribe S, Atkinson D, Eggers H, Sørensen, TS, Hansen MS, Razavi RS, Schaeffter T. Whole-heart imaging using undersampled radial phase encoding (RPE) and iterative sensitivity encoding (SENSE) reconstruction. Magn Reson Med 2009;62:1331–1337.

23. Pruessmann KP, Weiger M, Börnert P, Boesiger P. Advances in sensitivity encoding with arbitrary k-space trajectories. Magn Reson Med 2001;46:638–651.

24. Winkelmann S, Schaeffter T, Koehler T, Eggers H, Doessel O. An optimal radial profile order based on the golden ratio for time-resolved MRI. IEEE Trans Med Imaging 2007;26:68–76.

25. Buerger C, Clough RE, King AP, Schaeffter T, Prieto C. Nonrigid motion modeling of the liver from 3-D undersampled self-gated golden-radial phase encoded MRI. IEEE Trans Med Imaging 2012;31:805–815

26. Lustig M, Donoho D, Pauly JM. Sparse MRI: the application of compressed sensing for rapid MR imaging. Magn Reson Med 2007;58:1182–1195.

27. Otazo R, Kim D, Axel L, Sodickson DK. Combination of compressed sensing and parallel imaging for highly accelerated first-pass cardiac perfusion MRI. Magn Reson Med 2010;64:767–776.

28. Rasche V, Proksa R, Sinkus R, Bornert P, Eggers H. Resampling of data between arbitrary grids using convolution interpolation. IEEE Trans Med Imaging 1999;18:385–392.

29. Buerger C, Schaeffter T, King AP. Hierarchical adaptive local affine registration for fast and robust respiratory motion estimation. Med Image Anal 2011;15:551–564.

30. Schmidt JFM, Buehrer M, Boesiger P, Kozerke S. Nonrigid retrospective respiratory motion correction in whole-heart coronary MRA. Magn Reson Med 2011;66:1541–1549.

31. Good WF, Sumkin JH, Dash N, Johns CM, Zuley ML, Rockette HE, Gur D. Observer sensitivity to small differences: a multipoint rank order experiment. AJR Am J Roentgenol 1999;173:275–278.

32. Botnar RM, Stuber M, Danias PG, Kissinger KV, Manning WJ. Improved coronary artery definition with T2-weighted, free-breathing, three-dimensional coronary MRA. Circulation 1999;99:3139–3148

33. McGee KP, Manduca A, Felmlee JP, Riederer SJ, Ehman RL. Image metric-based correction (Autocorrection) of motion effects: analysis of image metrics. J Magn Reson Imaging 2000;11:174–181

34. Vuissoz P-A, Odille F, Fernandez B, Lohezic M, Benhadid A, Mandry D, Felblinger J. Free-breathing imaging of the heart using 2D cine-GRICS (generalized reconstruction by inversion of coupled systems) with assessment of ventricular volumes and function. J Magn Reson Imaging 2012;35:340–351.

35. Sorensen TS, Schaeffter T, Noe KO, Hansen MS. Accelerating the nonequispaced fast fourier transform on commodity graphics hardware. IEEE Trans Med Imaging 2008;27:538–547.

36. Doneva M, Stehning C, Nehrke K, Bornert P. Improving scan efficiency of respiratory gated imaging using compressed sensing with 3D Cartesian golden angle sampling. In Proceedings of the 19th Annual Meeting ISMRM, Montreal, Canada, 2011. Abstract 641.

37. Cheng JY, Uecker M, Ally MT, Vasanawala SS, Pauly JM, Lustig M. Free-breathing pediatric imaging with nonrigid motion correction and parallel imaging. In Proceedings of the 21st Annual Meeting of ISMRM, Salt Lake City, Utah, USA, 2013. Abstract 312.

38. Odille F, Uribe S, Batchelor PG, Prieto C, Schaeffter T, Atkinson D. Model-based reconstruction for cardiac cine MRI without ECG or breathholding. Magn Reson Med 2010;63:1247–1257